THE ASTROPHYSICAL JOURNAL, 988:108 (16pp), 2025 July 20 https://doi.org/10.3847/1538-4357/addd09

Mother's Day Superstorms: Pre- and Post-storm Evolutionary Patterns of ARs 13664/8

Mausumi Dikpati[1], Marianna B. Korsós[2,3,4], Aimee A. Norton[5], Breno Raphaldini[1,6], Kiran Jain[7],
Scott W. McIntosh[8], Peter A. Gilman[1], Andre S. W. Teruya[6], and Nour E. Raouafi[9]
[1] High Altitude Observatory, NSF-NCAR, 3080 Center Green Drive, Boulder, CO 80301, USA; dikpati@ucar.edu
[2] School of Electrical and Electronic Engineering, University of Sheffield, Amy Johnson Building, Portobello Street, Sheffield, S1 3JD, UK
[3] Department of Astronomy, Eötvös Loránd University, Pázmány Péter sétány 1/A, H-1112 Budapest, Hungary
[4] Hungarian Solar Physics Foundation, Petőfi tér 3, H-5700 Gyula, Hungary
[5] Hansen Experimental Physics Laboratory, 452 Lomita Mall, Stanford, CA 94305-4085, USA
[6] Instituto de Astronomia, Geofísica e Ciências Atmosféricas, Universidade de São Paulo, São Paulo, Brazil
[7] National Solar Observatory, 3665 Discovery Dr., Boulder, CO 80303, USA
[8] Lynker Space, Boulder, CO 80301, USA
[9] Johns Hopkins Applied Physics Laboratory, Space Exploration Sector, 11100 Johns Hopkins Road, Laurel, MD 20723-6099, USA

Received 2025 March 21; revised 2025 May 23; accepted 2025 May 23; published 2025 July 17

Abstract

In the week including Mother's Day 2024, active region (AR) 13664 became superactive when AR 13668 emerged nearby, causing multiple X-class flares and coronal mass ejections, and an increase in activity level similar to that inferred from geomagnetic storms associated with the historic 1859 events. By analyzing both global warped toroids on which the active regions are strung, and active-region-scale magnetic flux and helicity, we find (i) the north and south toroids have nearly identical warped patterns, with mostly longitudinal wave numbers $m = 1$–3; (ii) in three longitude intervals the north and south toroids were tipped away from each other in latitude, with a longitude phase shift between them, creating locations most prone to AR eruptions; (iii) on an active region scale, vector magnetic fields deviate far from potential fields, and therefore contain large amounts of magnetic "free energy" available for conversion into kinetic energy and high-temperature radiation; (iv) the positive and negative polarities converge toward each other, facilitating reconnection and magnetic energy release; and (v) rapid changes in magnetic helicity, caused by helicity injection from below that creates helicity imbalances. Despite the coarser resolution of GONG magnetograms, the derived global toroids are strikingly similar to those derived from the Solar Dynamics Observatory's Helioseismic and Magnetic Imager. We conclude that the Mother's Day superstorms were caused by enhanced magnetic complexity occurring due to intricate interactions among multiple active regions emerging at nearly the same locations. This suggests that predicting the locations of magnetically complex active regions, and studying and tracking their eruptive states using different proxy parameters can greatly improve our ability to forecast intense storms, not only hours but potentially weeks in advance.

Unified Astronomy Thesaurus concepts: Solar active regions (1974); Solar flares (1496); Solar activity (1475)

1. Introduction

Throughout 2024 May enigmatic solar storms and associated geomagnetic storms caused disruptions to ground-based broadcasting and radio communication systems. These storms, also known as the Gannon storm, produced intense auroras which were visible as low as 26° latitude, including Florida in the United States. During the present superactive phase of solar activity cycle 25, active regions (ARs) 13664/8, emerging at the south hemisphere of the Sun, caused 14 major coronal mass ejections (CMEs) during May 8–14. Initially, two active regions, AR 13663 and AR 13664, appeared in the north and south hemispheres of the Sun, respectively, on May 1 and 2. While two gigantic flares exploded from AR 13663, facing the Earth and causing shortwave radio blackouts in Australia, Japan, and China, AR 13664 in the meantime began growing to more than 15 times the Earth's size, similar to the one that caused the Carrington Event in 1859.

Within a few days AR 13668 emerged in close proximity to AR 13664 and commenced complex interactions. Both these active regions first appeared as β-type regions, but quickly turned into a δ-type configuration. Such a configuration is well known for intense eruptions and for producing powerful solar storms. During solar storms in 1989, Hydro-Québec power grids in Canada were negatively impacted, resulting in 9 hr of power outage. In the present case, various utilities and satellite operations, including those of Hydro-Québec, Transpower New Zealand Limited, various telecommunication companies in the United States, and NASA's ICESat-2, had prepared protection from the hazardous impact of these geomagnetic and solar superstorms. Despite this, Geostationary Operational Environmental Satellite 16 (GOES-16), a weather satellite operated by NASA and NOAA, stopped transmitting data for a few hours on May 13, and some drones, which rely heavily on GPS, were reported to have lost control and crashed.

Storms similar to the 2024 May superstorms occurred 20 yr ago, during the end of 2003 October, known as the Halloween storms. The 2024 May superstorms occurred through Mother's Day, and hence we refer to them as the Mother's Day superstorms. AR 13664 remained large and active for several weeks following the Mother's Day storms, and survived for an unusually long time —more than one Carrington rotation—coming to the front side again with a new name as AR 13697, and continuing to cause several more X-class flares from late May until mid-June.

Many questions arise: How did this active region AR 13664 grow so large? Why was its lifetime so long? This active region rotated to the back side and came back again to the front side without substantially decaying: What are its associated global and local evolving magnetic patterns? Where is the origin of such a large sunspot region? Obviously, so many questions cannot be answered in one study. This active region will certainly remain under investigation for many years.

Several recent studies have addressed different aspects concerning AR 13664, including general aspects of X-class flares (Y. Li et al. 2024), the resulting geomagnetic storms (Y. D. Liu et al. 2024; H. Hayakawa et al. 2025), and radio bursts associated with X-class flares (O. Kruparova et al. 2024). Characteristics of the magnetic flux emergence and flows leading up to the complex magnetic field structures were investigated by P. Romano et al. (2024). By analyzing the time evolution of the emerging magnetic fluxes and horizontal photospheric motions, it was concluded that a combination of sequential emergences of magnetic bipoles with convergence and shear motions lead to configurations favorable for intense flare activity.

Of late, the global dynamics of active regions' spatiotemporal distribution is being explored, utilizing extensive magnetogram observations. Such studies reveal important pre-solar-storm features that can provide clues for upcoming big flares and/or CMEs. For example, M. Dikpati et al. (2021) showed that the active regions do not emerge on the surface in a fully random fashion; instead, analysis of their latitude–longitude locations at the surface indicates that they manifest in a tight-fit toroid pattern (see also A. A. Norton & P. A. Gilman 2005). During the Halloween storms, two toroid patterns in the north and south hemispheres to which the active regions were tightly connected revealed that the north and south toroids tipped away from each other at certain longitudes and came closer to each other at certain other longitudes. It was argued there that the active regions manifesting at the tipped-away portions of the toroids in the north and south can strengthen themselves during the course of their evolution, and become susceptible to eruptions in the form of CMEs and flares. On the other hand, since the magnetic field directions are opposite in these toroids in the two hemispheres, coming closer to and sometimes overlapping on each other could cause annihilation and hence weakening of the active regions emerging at the locations of the warped toroids, making those locations much less likely for eruptions. The Halloween storms, produced from active regions AR 10486 in the south hemisphere and AR 10484 in the north hemisphere, emerged at the tipped-away portions of the toroids.

Subsequent analysis of active regions' global patterns during cycles 24 and 25 have further validated this concept. B. Raphaldini et al. (2023) showed that the second-biggest X-class flare in cycle 24 was caused by AR 11263 appearing in the north hemisphere at a longitude interval which was tipped away from the south toroid.

The authors also showed that the tipping pattern between north and south toroids quite often forms more than a Carrington rotation before the active regions manifest there and subsequently erupt as CMEs and flares. A plausible scenario for the physics behind such a tipping pattern of active regions' distribution observed at the surface is the tipping instability of dynamo-generated, spot-producing toroidal rings at/near the subadiabatically stratified base of the convection zone or the tachocline (P. S. Cally et al. 2003; M. S. Miesch et al. 2007). The tipping instability is an extremely robust feature of magneto-shear instability in 2D, quasi-3D shallow-water-type, and 3D thin-shell models. If the tipped-away parts of the toroids in the north and/or south coincide with fluid bulges (or high-pressure regions, i.e., regions where there is a positive departure from equilibrium pressure), the magnetic flux at those regions enters the turbulent convection zone and becomes prone to emergence at the surface. In the case of quasi-3D and 3D models, these positive pressure-departure regions are associated with the fluid bulges, which provide additional stimuli for the flux emergence from these locations.

A complementary view to the global aspects that lead to enhanced flare activity is that of the short-term, small-scale dynamics of these active regions, which have been studied using magnetic helicity (M. A. Berger & G. B. Field 1984; M. A. Berger 1999; D. MacTaggart & C. Prior 2021; E. Liokati et al. 2022, 2023). Magnetic helicity is a measure of the complexity of a magnetic field configurations that is widely used in the study of magnetic field emergence in active regions.

In this paper, we derive pre- and post-solar-storm structures for the north and south toroids (or N and S toroids, respectively), the latter containing ARs 13664/8, which caused solar and geomagnetic superstorms with multiple X-class flares and associated threats to our technological society (at the same time causing the most beautiful northern and southern lights for over 500 years, widely seen in various parts of the world). Our aim is to uncover the specific features of ARs 13664/8 during its evolution through multiple Carrington rotations, and identify the ones that reveal important predictive capability in advance of upcoming superstorms.

2. Methodology for Analysis of Global and Local Dynamics of ARs 13664/8

2.1. Derivation of Global Distribution Patterns of Active Regions from Magnetograms

Magnetograms reveal that the occurrence of active regions on the photosphere is not random; instead, they are tightly strung in warped toroids (A. A. Norton & P. A. Gilman 2005; M. Dikpati et al. 2021) in narrow latitude belts in each hemisphere. These warped toroids drift toward the equator with the progress of a solar cycle. Such an organized spatiotemporal evolutionary pattern indicates their deep origin, probably at the convection zone base or tachocline, which is more subadiabatically stratified than the turbulent convection zone. Irrespective of their origins, we can derive these warped toroid patterns containing active regions, by employing a technique called the trust-region reflective (TRR) algorithm. A TRR is essentially a nonlinear optimization technique which fits the centroids of active regions' flux by the combination of Fourier modes. Basically, when a high-dimensional functional space is replaced by a function that is significantly simpler, such as Fourier modes here in the parameter space of our interest, a "trust region" is defined in that space by such objective functions. The departures in these functions are iteratively minimized over the trust region, and when a local minimum is reached, the algorithm expands the parameter space of the trust region until there is a convergence. We have found that the warped toroid patterns on which active regions tightly fit can be derived for combinations of low longitudinal wavenumber modes; for our purposes, up to $m = 10$ modes are sufficient.

We have already described the formulation of the TRR algorithm in detail (M. Dikpati et al. 2021), and have applied it to derive toroids in peak-phase storms of cycles 23, 24, and 25 (B. Raphaldini et al. 2023, 2024). We briefly reproduce the mathematical formulation here. The TRR technique utilizes the latitude–longitude (θ, ϕ) distribution of the line-of-sight magnetic fields in the daily Solar Dynamics Observatory (SDO) Helioseismic and Magnetic Imager (HMI) synoptic magnetograms, deriving the best fit by optimizing the distributions of the centroids of unsigned flux as follows:

$$P_c(\phi, t) = q_0(t) + \sum_{m=0}^{N} q_m(t)\sin(m\phi + \zeta_m(t)), \tag{1}$$

$$q_m(t) = \overline{q_m}\left[1 + \sum_{m=0}^{N} s_{i,m}(t)^i\right], \tag{2}$$

$$\zeta_m(t) = \overline{\zeta_m}\left[1 + \sum_{m=0}^{N} w_{i,m}(t)^i\right]. \tag{3}$$

Here $P_c(\phi, t)$ denotes the central latitude of the toroid, which is a function of longitude and a slowly varying function of time, and $q_m(t)$ and $\zeta_m(t)$ denote the amplitude and phase of the mth mode, respectively (M. A. Branch et al. 1999; M. Dikpati et al. 2021). Here t is in units of 1 day, because we are analyzing daily synoptic magnetograms here.

2.2. Magnetic Helicity Calculations

Magnetic helicity (H_M) is an important quantity in magnetohydrodynamic (MHD) systems, being conserved in ideal MHD and even in dissipative cases typically dissipated at a much slower rate than energy (W. M. Elsasser 1956; M. A. Berger & G. B. Field 1984). Magnetic helicity is expressed by $H_M = \int_\Omega \boldsymbol{B}\ .\ \boldsymbol{A} d^3\boldsymbol{x}$, where $\boldsymbol{B}$ represents the magnetic field and $\boldsymbol{A}$ represents the vector potential defined on a volume Ω. The role of magnetic helicity in the context of predicting upcoming flares has been discussed in detail in B. Raphaldini et al. (2023, 2024). Here we briefly mention the calculation setup after providing the physical interpretation of how the evolution of helicity could hint at possible eruptions.

H_M in general represents the magnetic field's topology in terms of the linking number (i.e., the number of crossings between a pair of closed magnetic loops) weighted by the magnetic flux, twist (i.e., the rotation of a magnetic flux tube around its axis), and writhe (i.e., the rotation or bending of the flux tube's axis itself). Calculating the magnetic helicity from solar magnetic field observations poses challenges, since observations are usually available on the surface represented by the photosphere; furthermore, the vector potential is not gauge invariant. A possible way to overcome these problems is first to work with the concept of relative helicity, namely the helicity calculated relative to a reference potential field, given by $H_P = \int_\Omega (\boldsymbol{B} - \boldsymbol{B}_P) \cdot (\boldsymbol{A} - \boldsymbol{A}_P) d^3\boldsymbol{x}$, where the subscripts $\boldsymbol{B}_P$ and $\boldsymbol{A}_P$ denote a potential magnetic field with its vertical component coinciding with the magnetogram observations and the respective vector potential. A second step is to calculate the helicity fluxes through the photospheric surface. A comprehensive discussion of relative helicity in various configurations of magnetic fields in multiply connected domains can be found in D. MacTaggart & A. Valli (2023). Here we briefly produce the mathematical prescriptions used to derive our results.

Considering a portion of the photospheric surface $\partial\Omega$, the helicity flux up to a time T is given by

$$H = -\frac{1}{2\pi}\int_0^T \int_{\partial\Omega}\int_{\partial\Omega} B_z(\boldsymbol{x})B_z(\boldsymbol{y}) \times \frac{(\boldsymbol{u}(\boldsymbol{x}) - \boldsymbol{u}(\boldsymbol{y}))(\boldsymbol{x} - \boldsymbol{y})}{|\boldsymbol{x} - \boldsymbol{y}|^2} d^2x d^2y dt, \tag{4}$$

in which x and y are points on the photospheric surface, and $\boldsymbol{u}$ is the field line velocity. The respective helicity density flux at point x is given by

$$\frac{d\mathcal{H}(\boldsymbol{x})}{dt} = -\frac{1}{2\pi}\int_{\partial\Omega} B_z(\boldsymbol{x})B_z(\boldsymbol{y}) \times \frac{(\boldsymbol{u}(\boldsymbol{x}) - \boldsymbol{u}(\boldsymbol{y})) \times (\boldsymbol{x} - \boldsymbol{y})}{|\boldsymbol{x} - \boldsymbol{y}|^2} d^2y. \tag{5}$$

By defining a potential magnetic field B_p with its $\hat{z}$-component coinciding with B_z, we can further decompose both the accumulated helicity and the helicity density flux into their current-carrying and potential components. This is done by decomposing the velocity in the following way:

$$\boldsymbol{u}_c = \boldsymbol{v}_\| - \frac{v_z}{B_z}\boldsymbol{B}_{\|c};\ \ \boldsymbol{u}_p = \boldsymbol{v}_\| - \frac{v_z}{B_z}\boldsymbol{B}_{\|p}. \tag{6}$$

Here $\boldsymbol{v}_{||}$ is the in-plane plasma velocity, and $\boldsymbol{B}_{||p}$ and $\boldsymbol{B}_{||c}$ are the in-plane components of the potential and current-carrying magnetic field, respectively. Upon substituting in Equation (4) $\boldsymbol{u} \rightarrow \boldsymbol{u}_c$ and $\boldsymbol{u} \rightarrow \boldsymbol{u}_p$, we obtain the current-carrying helicity component and its density flux (H_c and $d\mathcal{H}_c(\boldsymbol{x})/dt$, respectively) and the potential helicity component (H_p and $d\mathcal{H}_p(\boldsymbol{x})/dt$, respectively).

A parameter $\delta H'$ was recently introduced by B. Raphaldini et al. (2022) to quantify the degree of potential/current-carrying helicity injection, or in other words the helicity imbalance:

$$\delta H' = \int_{\partial\Omega}\left(\left|\frac{d}{dt}\mathcal{H}_c(\boldsymbol{x})\right| - \left|\frac{d}{dt}\mathcal{H}_p(\boldsymbol{x})\right|\right)d^2\boldsymbol{x}. \tag{7}$$

Positive values of $\delta H'$ indicate helicity injection dominated by current-carrying structure, while negative values of $\delta H'$ indicate the dominance of potential magnetic field structure. The associated density is defined as

$$\delta\mathcal{H}' = \left(\left|\frac{d}{dt}\mathcal{H}_c(\boldsymbol{x})\right| - \left|\frac{d}{dt}\mathcal{H}_p(\boldsymbol{x})\right|\right). \tag{8}$$

Intuitively, one can understand the relationship between the injection of magnetic helicity and the occurrence of strong flares as a manifestation of the complexity of the emerging magnetic fields. S. Toriumi & S.-H. Park (2024) provides a comprehensive physical foundation about how magnetic helicity injection could indicate the occurrence of active region eruptions leading to CMEs and flares. The more entangled the emerging field is (in terms of its linkage) and the stronger the magnetic fluxes, the more likely it is that these magnetic structures are prone to explosive releases of energy associated with magnetic reconnection events. Fast emergence of complex magnetic structures through the photosphere will manifest themselves as an increased rate of helicity injection. The helicity imbalance addresses another important aspect, which is the need for substantial current-carrying magnetic field in order for energy to be available to be dissipated. Spikes in the helicity imbalance are usually indicative of significant imminent flare activity.

3. Results

AR 13664 appeared on the disk on 2024 April 30, initially with a simple β configuration. The region continued to be classified as β until May 2, already producing its first C-class flares starting May 1. On May 3, AR 13664 evolved into a more complex $\beta - \delta$ structure, producing a pair of M-class flares, the first of many. On May 5, another pair of M-class flares was observed, while the active region maintained its $\beta - \delta$ structure. On May 6, the active region evolved into a $\beta - \gamma - \delta$ structure, followed by a dramatic increase in flare activity on May 7, including M-class flares at a frequent rate. The first X-class flare was produced on May 8, a X-1.02 flare, already at the western part of the disk. From May 8 until its transit to the limb on May 14, a total of 12 X-class flares, the largest of which was a X-8.79 flare, already on the limb on May 14.

To analyze the May superstorms, we first derive the evolutionary patterns in the global distribution of active regions, and study the features of these warped toroids.

3.1. Global Dynamical Evolution of Toroids Containing ARs 13664/8

3.1.1. Weekly Evolution of Global Toroid Patterns from SDO/HMI Data before, during, and after Mother's Day Superstorms

To derive global toroid patterns we implement the algorithm described in Section 2.1 on SDO/HMI data as well as on GONG data. The purpose of showing at least one case, namely the "Mother's Day" toroids, derived using GONG magnetograms is to demonstrate that GONG data, despite its much lower resolution (360 × 180 pixels), can roughly complement the data gap (if any) in SDO/HMI. We obtain the SDO/HMI magnetogram daily fits files from JSOC. These synoptic maps of the magnetic field are updated daily and are created by averaging values over a 4 hr period within 60° of the central meridian. When a specific Carrington longitude moves out of this central region, the magnetic field values remain constant until it reenters the central part of the disk. This process results in an image with a resolution of 3600 × 1440 pixels.

Figure 1 shows the weekly evolution of global toroid patterns from April 23 to May 21, covering the period from a week before the emergence of AR 13664 and a week after all the major events of the Mother's Day superstorms. Upon examination of panels (a)–(f) of Figure 1, from the top to the bottom, a few features immediately become evident. First, the toroids are seen to evolve very slowly over 5 weeks. This is not surprising, because the most likely governing mechanism for the evolution of these toroids is the nonlinear interactions among the dynamo-generated toroidal magnetic fields, differential rotation, and magnetically modified Rossby waves. We have described the physics in the case of the Halloween storms (M. Dikpati et al. 2021). Because the Rossby waves' drift speed in longitude is very low, the toroids seem to be almost static in the rotating frame of the Sun for a few weeks.

Second, both the north and south toroids exhibit nearly identical warped patterns, formed by a combination of three dominant large-scale longitudinal modes with wavenumbers $m = 1, 2, 3$. These patterns display a primarily antisymmetric tip about the equator, with the N and S toroids tipping away from each other in certain longitude intervals, but there is in addition a small, overall phase shift between them. The N and S toroids are tipped away from each other in three different longitudinal regions (e.g., approximately 170°–210°, 240°–310°, and 340°–80° through 0°, i.e., 340°–360° and 0°–80°). As a result, this configuration creates regions within the toroidal band that are more prone to erupt in the form of big flares/or CMEs. Note that the amount of the tip between N and S toroids can be extremely enhanced in a purely antisymmetric-type tipping pattern; in such cases, more often there also exists longitude intervals where the N and S toroids overlap. On the other hand, the tip amount gets reduced if there exists a longitudinal phase shift between the two toroids, despite each having a purely antisymmetric tip. Based on these patterns, various scenarios can form for creating the possibility of active region eruptions depending on their locations of emergence. How multiple global pattern scenarios can lead to the best to least possibility of eruption is discussed in detail in Sections 3.1.2.

Third, AR 13664 emerged at an absolute longitude of 350° in the south toroid, where there was a decaying active region, AR 13613, the presence of which was an additional stimulant for triggering complex interactions between the decayed AR and the new emergence there. We have already seen, in the case of the 2017 solar storms produced from the biggest flare of cycle 24, that a new active region can emerge from the location of an apparently decaying active region, AR 12673, turning AR 12673 into the most active region of that cycle. While AR 13664 had already started erupting in the form of C-class flares and associated CMEs from May 1, it turned into a superactive one after the complex interactions with AR 13668, which emerged at 337° longitude on May 6 in the close proximity of AR 13664. Therefore, it will be more accurate to consider ARs 13664/8 together as the superactive regions that were responsible for the Mother's Day superstorms.

The fourth feature we find from Figure 1 is that ARs 13664/8 never experienced weakening through annihilating interaction with an active region in the same location in the north toroid. The active regions in the adjacent longitudes in the north toroids are at 290° and 30°, respectively. In fact, most of the flaring active regions are primarily in the alternating longitude locations in the north toroid with respect to the south. This feature is much better revealed in the top panel of Figure 2, which we discuss in more detail in the next subsection.

3.1.2. Comparison between Toroid Patterns Derived from SDO/HMI and GONG Magnetograms

As mentioned in Section 3.1.1, it is prudent to perform the same analysis using multiple data sources. The resolution of GONG magnetograms is much lower than SDO/HMI magnetograms. The openly accessible fits files for GONG magnetograms are 360 × 180 pixels in longitude and latitude, respectively. Because our goal here is to analyze the global toroid patterns, coarse resolution may not be a problem. One advantage of GONG magnetograms is that the latitude extent is from −90° to +90°, larger compared to the SDO/HMI magnetograms.

In Figure 2, we show in the top panel the toroid patterns for May 14 derived from SDO/HMI data; the bottom panel displays the corresponding toroid patterns derived from GONG data. The top panel is essentially the panel (e) of

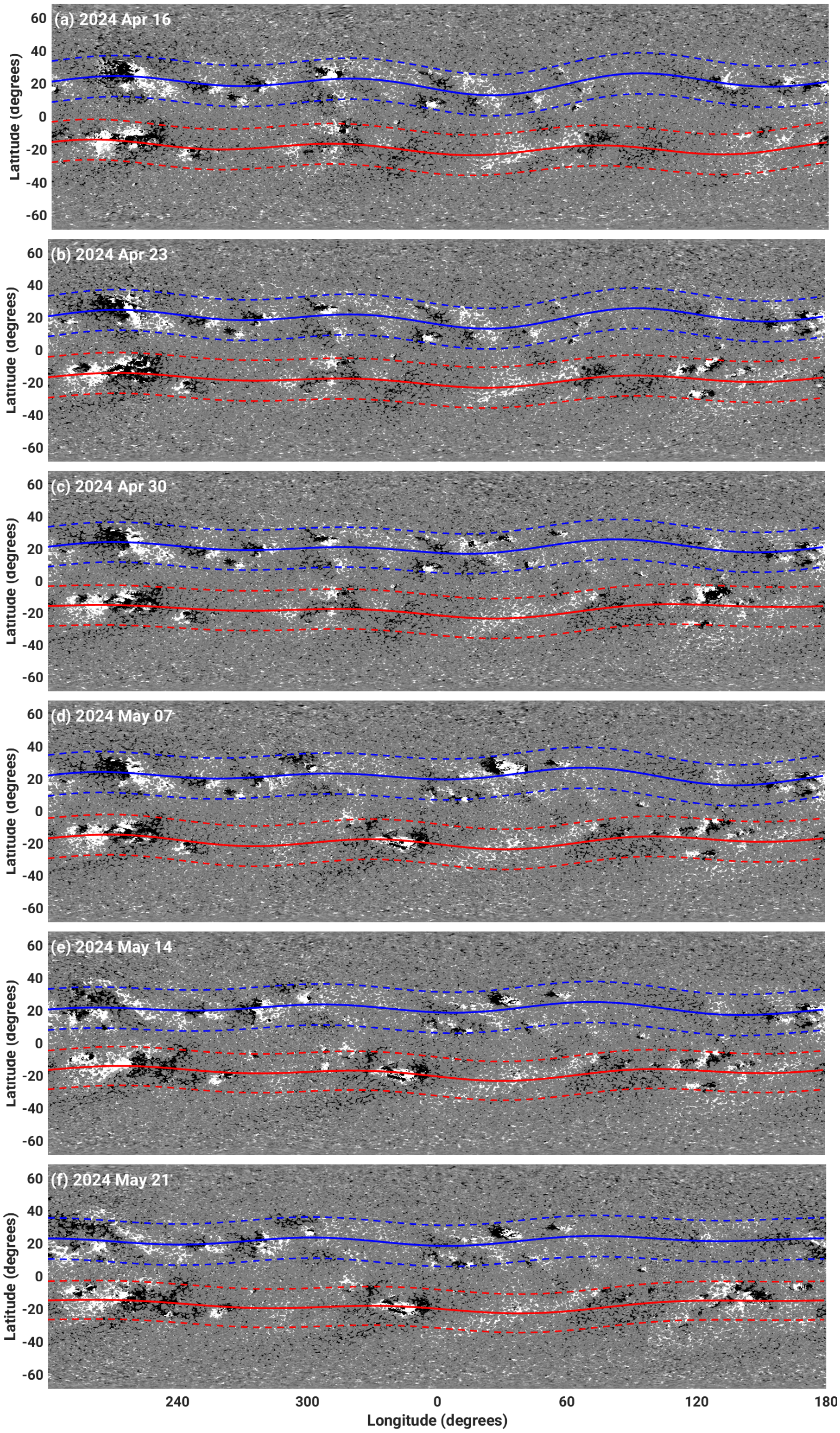

Figure 1. Panels (a)–(f), from top to bottom, display the evolution of global toroid patterns in the interval of a week, before, during, and after the Mother's Day superstorms. Blue and red solid curves indicate the central latitudes of the north and south toroids, respectively, whereas dashed blue (red) curves on both sides of solid blue (red) curves indicate the latitudinal widths of the toroids, in which the active regions are tightly strung. Active region(s) ARs 13664/8 emerged at an absolute longitude of 350°, and can be prominently seen from panel (d) onward.

Figure 1, except that we have circled and marked all the flaring active regions. Toroid patterns displayed in the bottom panel of Figure 2 reveal very similar global patterns, constructed as a combination of $m = 1$, 2 and 3 longitudinal modes. We find the same tipping pattern in the bottom panel as in the top panel. The bandwidth of the toroids derived from GONG data appears slightly broader than that derived from SDO/HMI data. This is not surprising, because the pixels in both the latitude and longitude dimensions are about 10 times coarser in the case of GONG data compared to SDO/HMI data, and the

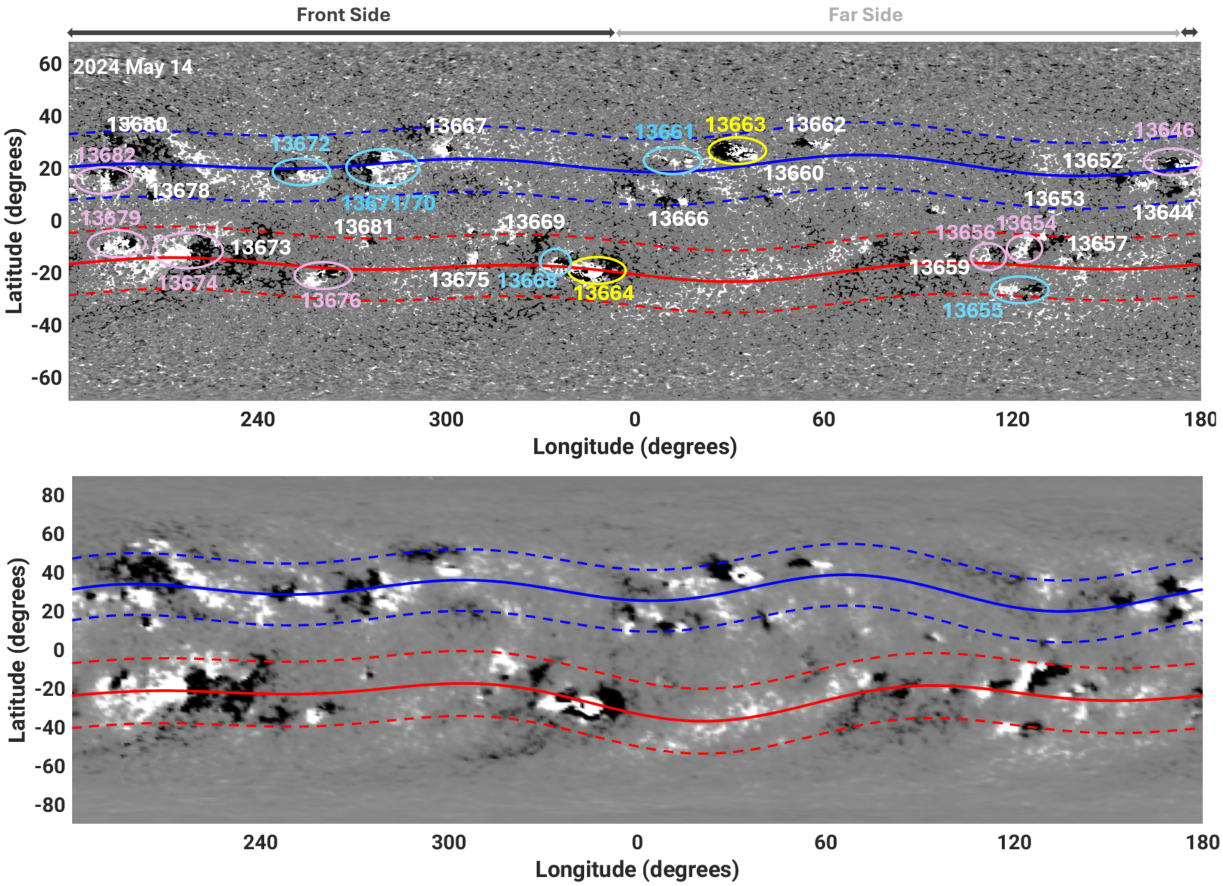

Figure 2. Top: all flare-producing active regions are identified with NOAA numbers for the May 14 global toroid patterns, derived from SDO/HMI data; yellow-circled ARs produced X-class flares, magenta-circled ARs M-class flares, and cyan-circled ARs C-class flares. Nonflaring ARs are not circled, but they have been identified in white text with NOAA numbers. Bottom: May 14 toroid patterns derived from GONG data. Note that the latitude range in the GONG fits files is larger than the SDO/HMI fits files.

width of the toroids originates from the statistical spread in the optimization method. Thus, a coarser resolution of the data is expected to result in a larger spread, and hence a larger width of the toroids. Nevertheless, comparison of the top and bottom panels reveals that GONG data also provide a faithful derivation of the toroid patterns on which active regions are tightly strung. The larger latitude dimension in the GONG data is reflected in the larger aspect ratio of latitude versus longitude in the bottom panel.

We see from the analysis of the spatiotemporal evolution of these global toroid patterns in the present study, as well as in our previous studies performed for the big storms of cycles 23 and 24, that the pre-solar-storm active regions' distribution patterns can provide potential insights for upcoming eruptions and associated solar energetic events leading to large flares, especially if the active regions are turning into complex $\beta - \gamma - \delta$ configurations in certain spatial locations.

We explicitly discuss the scenarios for the locations of active region emergence in relation to the possibility of their eruptions. We have studied so far only six cases. Namely, M. Dikpati et al. (2021) explored the global dynamical evolutionary patterns of AR 10486 and AR 10488, which emerged in the perfectly tipped-away portions of the south and north toroids, and produced the Halloween storms during the peak phase of cycle 23 (i.e., the phase covering a few years around the cycle peak). B. Raphaldini et al. (2023) explored local dynamics as well as the global toroid patterns of AR 11263 and AR 11266—both located in the N toroid in portions tipped away from and toward the S toroid, producing the second-biggest flare and no flare in the cycle 24 peak phase, respectively. B. Raphaldini et al. (2024) studied ARs 13513/4 and AR 13590, which produced big X-class flares during the cycle 25 peak phase.

This is a small number for building thorough and extensive statistics, but these six cases still provide a reasonable consistency with respect to the scenarios that are displayed in Figure 3. The top panel displays a synthetic case of a pure antisymmetric tip of primarily $m = 2$ type; there occur two longitude intervals where the north and south toroids are tipped away from each other. This means when the N toroid is tipped away from the equator in a certain longitude range, the S toroid is also tipped away from the equator, creating a large separation in latitude between them in that longitude interval. The active regions, noted by gray-filled circles, appearing in the tipped-away portions in one or both hemispheres could be the most flare prone. Conversely, in certain other longitude ranges they both are tipped toward the equator, creating an overlap between the N and S toroids. Active regions appearing in these longitudes may not erupt, because they may weaken themselves by annihilation processes due to their opposite-polarity magnetic fields. The middle panel displays a case where the N and S toroids are symmetrically tipped, that is when the N toroid is tipped away from the equator, the S toroid is tipped toward the equator, and vice versa. This is also an

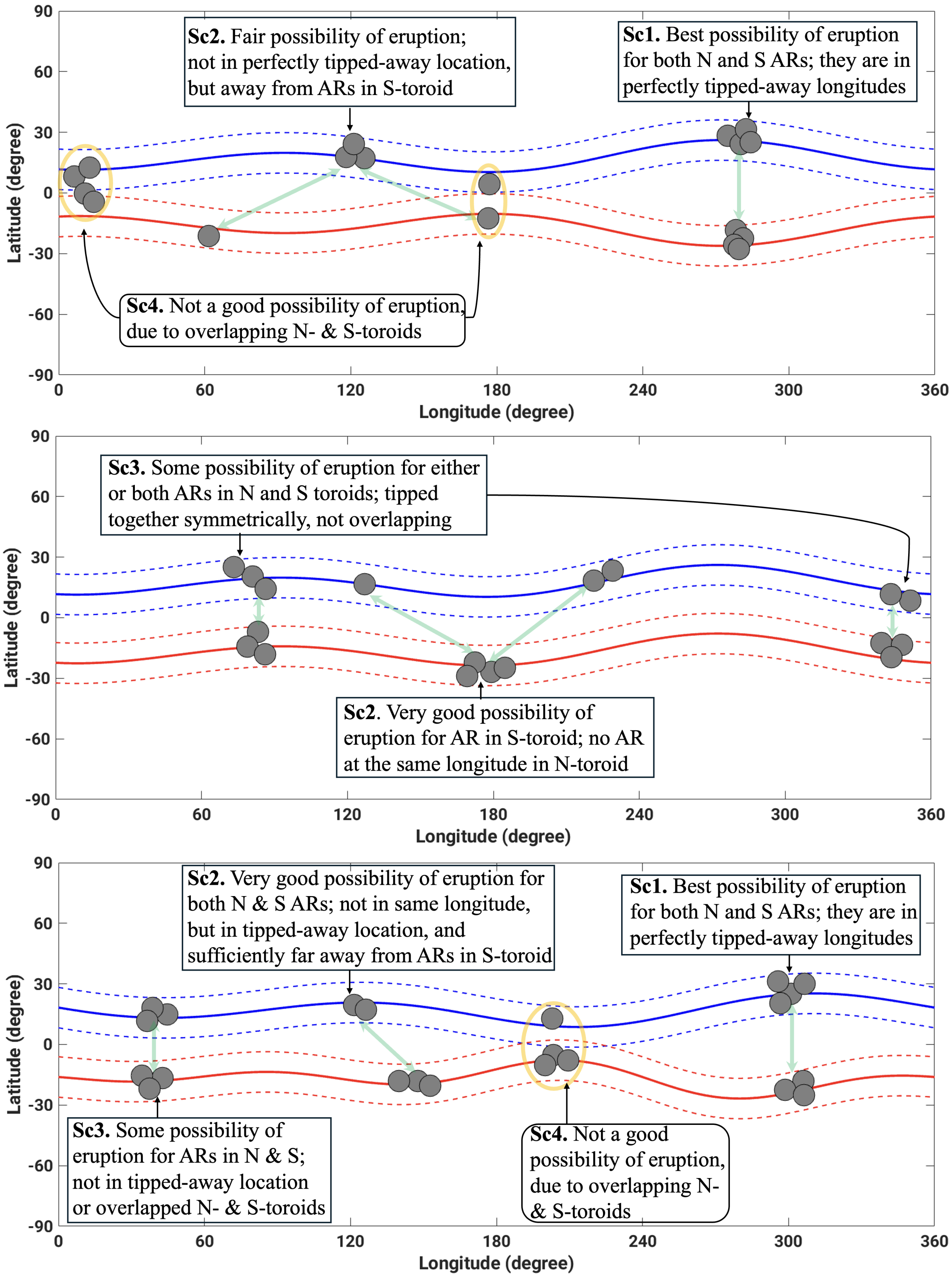

Figure 3. Toroids are schematically displayed in each panel by blue (north) and red (south). Solid curves denote the central latitude of the toroid as a function of longitude, and the two dashed curves for each toroid denote the latitudinal widths of the toroids. Gray-filled circles denote the locations of emerged active regions. Top: purely antisymmetric tipping between the north and south toroids, very much like the Halloween storms toroid patterns during cycle 23. Middle: symmetric tipping of the north and south toroids, similar to that found in the case of the second-biggest X-class flares during cycle 24. Bottom: mixed tipping patterns between north and south toroids, as seen in the case of cycle 25 storms in the late rising phase.

$m = 2$ type, but having a symmetric wavy pattern. Thus, they maintain a certain constant latitude separation between them at all longitudes. If active regions appear in one hemisphere at a certain longitude, there could be good chances of eruption; active regions in both hemispheres at the same longitude could still create some possibility of eruption, particularly when they

Table 1
All the Active Regions during 2024 April 16–May 23

Hemisphere	Active Region			Strongest Flare				Closest Scenario
	Number	Location lat_{hg}, $\text{long}_{\text{Carr}}$	Flares Produced	Flare Class	Active Region Details on Flaring Day[a]			
					Date	Configuration	Area (μ Hemi)	
North								
	AR 13644	13, 182	None	None	Apr 21	β	21	3
	AR 13646	22, 174	1 M, 2 C	M1.6	Apr 22	β	100	3
	AR 13652	14, 171	None	None	Apr 22	β	120	3
	AR 13653	3, 132	None	None	Apr 21	α	10	3
	AR 13660	11, 49	None	None	Apr 27	α	30	2
	AR 13661	22, 21	1 C	C3.1	Apr 29	α	30	2
	AR 13662	30, 60	None	None	May 3	β	100	2
	AR 13663	25, 38	5 X, 35 M, 40 C	X4.5	May 6	$\beta - \gamma - \delta$	600	2
	AR 13666	7, 18	None	None	May 4	β	130	2
	AR 13667	27, 307	None	None	May 7	α	150	2
	AR 13670	20, 284	2 C	C9.9	May 15	$\beta - \gamma$	20	2
	AR 13671	21, 285	1 C	C4.8	May 17	β	10	2
	AR 13672	19, 258	3 C	C7.1	May 11	β	140	2
	AR 13678	9, 214	None	None	May 10	α	10	3
	AR 13680	18, 201	None	None	May 13	β	30	3
	AR 13682	15, 282	1 M	M4.4	May 14	$\beta - \gamma$	130	3
South								
	AR 13654	−7, 136	11 M, 19 C	M9.5	Apr 30	$\beta - \delta$	550	3
	AR 13655	−28, 129	1 C	⋯	Apr 21	β	130	3
	AR 13656	−12, 118	2 M	M2.8	Apr 25	β	30	3
	AR 13657	−13, 144	None	None	Apr 25	β	10	3
	AR 13659	−13, 106	None	None	Apr 25	α	10	3
	AR 13664	−17, 350	9 X, 52 M, 33 C	X5.8[b]	May 11	$\beta - \gamma - \delta$	2400	2
	AR 13668	−17, 339	3 C, 4 M	M3.3	May 7	$\beta - \gamma$	50	2
	AR 13669	−9, 326	None	None	May 5	α	10	2
	AR 13673	−11, 235	None	None	May 12	α	30	3
	AR 13674	−12, 222	1 M, 2 C	M1.0	May 13	β	110	3
	AR 13675	−15, 316	None	None	May 13	$\beta - \gamma$	140	3
	AR 13676	−22, 266	1 M, 1 C	M1.1	May 12	$\beta - \gamma$	80	2
	AR 13679	−9, 204	10 M, 33 C	M4.2	May 23	$\beta - \gamma - \delta$	500	3
	AR 13681	17, 196	None	None	May 13	β	30	2

Notes. Contains data for Carrington rotation periods 2256 and 2257. Note that the latitude, longitude, and configuration are recorded for the time of the flare. Data source: NOAA/SWPC solar activity reports.

[a] If the active region did not produce a flare, the details are provided when it reached its maximum area.

[b] The most intense flare recorded by GOES was an X8.7 event from this region, occurring behind the west limb on May 14.

are developing complex patterns. In this pattern, the possibility of no eruption signal is absent, since there is no overlap of the toroids. The bottom panel displays a mixed-mode pattern, where the N and S toroids are tipped away from each other at certain longitudes, such as around 300°, but also show symmetric tipping at certain other longitudes (0°–60°). Obviously, there are possibilities of eruption when the active regions appear in tipped-away parts with large and moderate latitude separations between the N and S toroids, and no eruption from the locations where the toroids overlap.

We summarize these global scenarios below, as well as present their local properties (locations, configurations, and area) in Table 1 to better elucidate why some active regions in Figure 2 fulfilling the same global scenario produced flares and some did not.

1. *Scenario 1.* If the active regions emerge in the perfectly tipped-away locations of the north and/or south toroids, they are most prone to eruption, particularly if they are evolving into complex configurations like $\beta - \gamma - \delta$. This situation occurred during the Halloween storms in cycle 23 (see, e.g., Figures 11(c)–(e) of M. Dikpati et al. 2021).
2. *Scenario 2.* If the active regions are in the tipped-away portions of the N and S toroids, even though they may not be in the location of maximum tip but have a large latitude separation with their opposite-hemisphere counterparts, they will still be very prone to eruptions when they are growing complex. This situation occurred in the top panel of Figure 2 for ARs 13664/8 and also for previously studied cases (see, e.g., Figures 1 and 5(b) of B. Raphaldini et al. 2023, 2024, respectively). Furthermore, ARs 13661, 3663, 13670/1, 13672, and 13676 also fulfilled this scenario, and produced flares. On the other hand, ARs 13660, 13662, 13666, and 13667 did not flare, despite fulfilling this scenario, primarily due to either smaller area and/or simple configurations. Only one curiosity appears, for AR 13661, which had neither a complex configuration nor big area, but erupted into a

C-class flare. Because this happened on the back side, it is difficult to understand how it erupted, but most likely the global toroid scenario 2 along with multiple eruptions from the adjacent AR 13663 caused a sympathetic eruption for AR 13661.

3. *Scenario 3.* When the active regions are in the symmetrically tipped-away part of one hemisphere's toroid, there can exist a fair possibility of eruptions as they become more complex. We saw such a scenario during the 2024 December 7 toroids (see, e.g., Figure A2 in the Appendix of B. Raphaldini et al. 2024), in which ARs 13490 and 13499 produced M-class flares, and we also see here in the top panel of Figure 2, where the magenta-circled active regions (ARs 13674, 13679, and 13682 on the extreme left, and ARs 13646, 13654, and 13656 on the extreme right) erupted, producing M-class flares. In contrast, ARs 13644, 13652, 13653, 13678, and 13680 in the north and ARs 13657, 13659, 13673, and 13675 in the south did not flare, because they never developed into big and complex configurations; furthermore, scenario 3 is only a moderate global scenario for the possibility of eruption.
4. *Scenario 4.* When the active regions are in a longitude range of overlapping N and S toroids, the possibility of flares from them is extremely poor. While this scenario is not met by any active region in Figure 2, a good example was seen during 2024 February 21, when a number of big and complex active regions, ARs 13565, 13567, 13572, and 13573, did not erupt (see, e.g, Figure A1 in the Appendix of B. Raphaldini et al. 2024).

The evolution of active regions and their global patterns occurs on multiple spatiotemporal scales. Short-timescale phenomena like flares/CMEs occur on timescales of minutes to hours, while intermediate-timescale phenomena like quasi-periodic enhanced-activity bursts, more widely known as Rieger-type periodicity or quasi-biennial oscillations, occur on timescales of weeks to months. Predicting imminent intense flares and/or CMEs, occurring from the eruptions of active regions, involves knowledge about small-scale dynamics of active regions on timescale of minutes to hours (M. G. Bobra & S. Couvidat 2015; M. G. Bobra & S. Ilonidis 2016). On the other hand, the quasi-annual/quasi-biennial enhanced-activity bursts are intrinsically linked with the "seasons of space weather," which show an increased likelihood of intense flares during the peaks of the short-term activity bursts, mimicking a similar quasi-annual periodicity. The physical foundation for producing organized, slowly evolving global toroid patterns relies on Rossby waves' interactions with solar differential rotation and dynamo-generated magnetic fields in the tachocline (M. Dikpati & S. W. McIntosh 2020). These can create conditions for recurrent emergence of magnetic flux at the same locations of latitude–longitude; complex interactions among old and new active regions there could lead to multiple intense flares. However, as already extensively discussed in M. G. Bobra & S. Couvidat (2015) and M. G. Bobra & S. Ilonidis (2016), there is no single physical quantity that can provide the prediction of an upcoming flare/CME with 100% reliability.

This is why we must consider both the local and global pre-solar-storm dynamical features of flaring ARs. Taken together, they can improve the predictability of big storms. Therefore, we now discuss the local dynamics of ARs 13664/8 in Section 3.2.

3.2. Pre-solar-storm Local Dynamics of ARs 13664/8

3.2.1. Morphology and Evolution of ARs 13664/8

The ARs 13664/8 cluster showcased significant development and solar activity during its transit across the solar disk. This progression is detailed in Figure 4, which reports the AR 13664 and AR 13668 active regions, covering both the evolution of the regions and their flaring history. In Figure 4, the evolution of ARs 13664/8's morphology through continuum and magnetic field images can be visually observed. Initially spotted on the eastern limb of the Sun on May 1, AR 13664 expanded progressively as it moved across the solar disk.

The top frames of Figure 4 depict the configuration of ARs 13664/8 on May 5, highlighting moderate flux on the western side where the main polarities were rapidly separating, while smaller polarities underwent coalescence. On the eastern side, AR 13668 began to emerge with a relatively simple bipolar configuration, leading to an increase in the magnetic complexity of AR 13664, eventually classified as a $\beta - \delta$ configuration. This classification indicates significant magnetic complexity and potential for large flare activity. The magnetic classification system was put forward by G. E. Hale et al. (1919), and provides a simple way to point out various magnetic flux configurations in active regions. For example, a simple sunspot or spot group all having the same polarity is labeled an α configuration, whereas β denotes sunspots or spot groups that have two polarities. More complex configurations are γ and δ spots or spot groups, with γ-type spots containing intermixed polarity and δ-type active regions those that have at least one sunspot containing opposite magnetic polarities separated by $\leqslant 2°$ in heliographic distance inside of a common penumbra region. A detailed description of these classifications, along with interpretations about their behavior, can be found in S. A. Jaeggli & A. A. Norton (2016). Here we follow the designations as briefly described above to discuss our results.

By May 6, the active region had evolved into a $\beta - \gamma - \delta$ structure with multiple emerging bipoles on the eastern side adding flux to AR 13668, as shown in the middle frames of Figure 4. The nearly north–south alignment between the emerging flux of AR 13668 and the older AR 13664 sunspots increased the system's complexity. This was followed by a dramatic increase in magnetic flux emergence and flare activity on May 7, including frequent M-class flares. The first X-class flare, an X-1.02, occurred near the western part of the disk on May 8. By then the system had evolved into a very complex structure with multiple interacting and shearing bipoles, as shown in the bottom frames of Figure 4. This complex structure produced a total of 12 X-class flares before moving beyond the Sun's western limb on May 14, with the largest being an X8.79 flare.

3.2.2. Evolution of Helicity Several Hours before the Superstorms

First, the evolution of helicity in AR 13664 was studied, as introduced in B. Raphaldini et al. (2022), to better understand the relationship between the injection of magnetic helicity and the occurrence of strong flares, which serve as a manifestation of the complexity of the emerging magnetic fields. The more

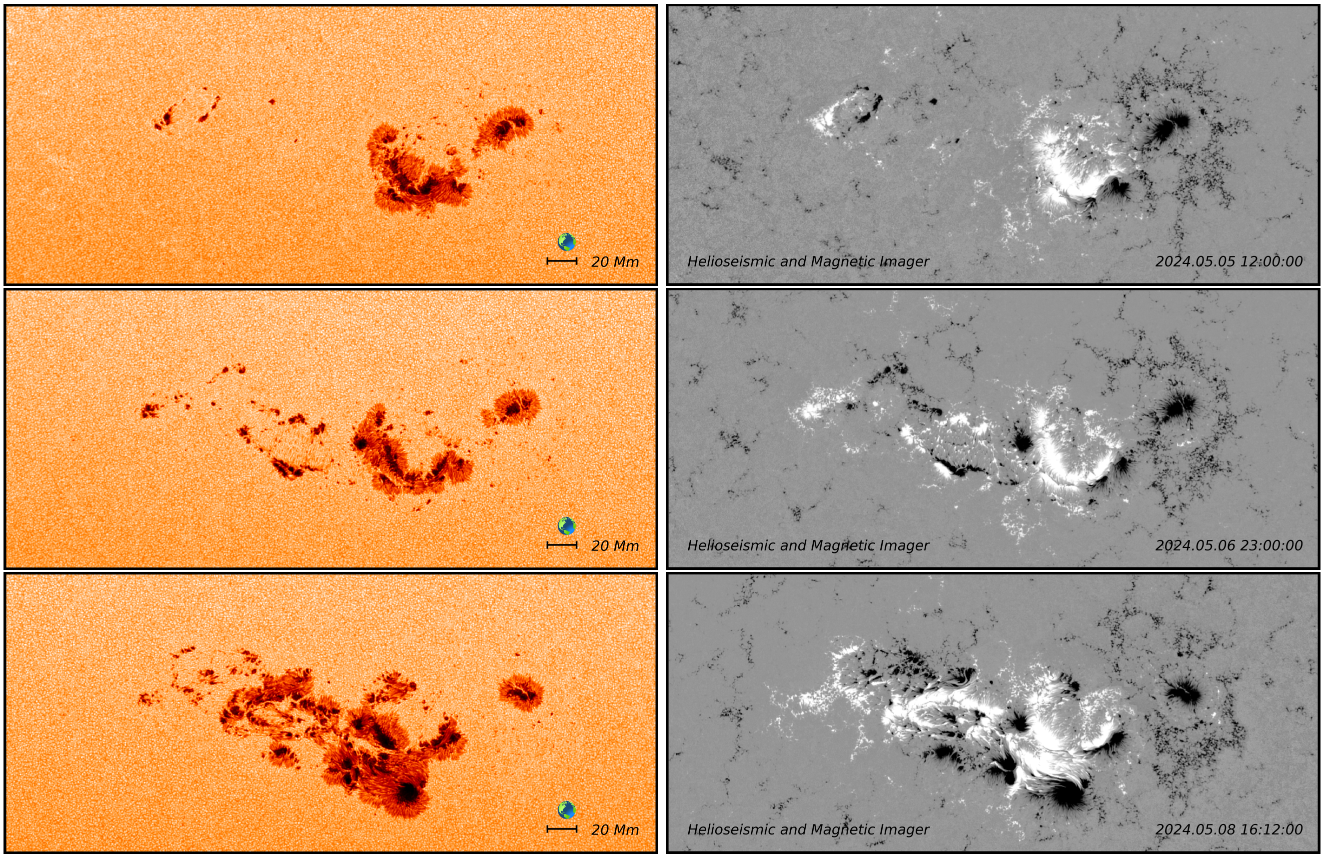

Figure 4. The evolution of the ARs 13664/8 cluster is shown with three snapshots from HMI continuum (left) and radial magnetic field (right) in cylindrical equal area projection. The active region at the right side of the first frame was denoted as AR 13664 first, with AR 13668 emerging to the east of it. Multiple pairs of bipoles emerged, with the positive and negative polarities seen in white and black, respectively. A movie of NOAA 13664/8 flux emergence is available online (https://vimeo.com/955625501).

entangled the emerging field is (in terms of its linkage) and the stronger the magnetic fluxes, the more likely it is that these magnetic structures are prone to explosive release of energy associated with magnetic reconnection events. Fast emergence of complex magnetic structures through the photosphere will manifest themselves as an increased rate of helicity injection. The helicity imbalance addresses another important aspect, which is the need for substantial current-carrying magnetic field in order for energy to be available to be dissipated.

The evolution of the magnetic helicity and helicity imbalance is shown in Figure 5. Time $t = 0$ is set as 2024 April 30. In the first ∼150 hr an almost steady injection of helicity is observed; while the overall accumulated helicities show a dominance of the current-carrying helicity, the helicity imbalance indicates a fluctuation around zero with a slight prevalence of positive values, confirming that on average more current-carrying helicity is being injected. At around $t = 160$ hr, the helicity values reach a plateau before slightly decreasing. Negative values in the helicity imbalance are observed after that, at around 175 hr, indicating injection of predominantly potential helicity. Starting at around $t = 200$ hr, we observe a steep increase in the helicity values, dominated by current-carrying helicity, while the helicity imbalance shows a sharp increase. Following this spike in the helicity imbalance, we observe the first X-class flare at around $t = 210$ hr. Subsequently, the helicity values increase steadily, maintaining the dominance of the current-carrying field, while the helicity imbalance stays overwhelmingly positive throughout this flare prolific interval. Five more X-class flares are observed before the active region approaches the limb, the largest of which is a X-5.89 flare on May 11 ($t \sim 210$) hr. After 60° of Carrington longitude data are discarded, since after that relative errors become larger, however six more X-class flares were produced.

3.2.3. Identifying and Evaluating Evolution of Flare Parameters

We further parameterize the evolution of ARs 13664/8 and provide deeper insight into their highly eruptive activity. First, by collecting data from the HELIO website,[10] we present in Figure 6 the evolution of the area of ARs 13664 and 13668. The two ARs interacted for a few days (from slightly before May 6 until slightly after May 9). This interaction caused the increase in complexity of AR 13664, as shown by the dashed red line in the top panel of Figure 6. In fact, AR 13668 behaved more like a catalyst to increase the complexity of AR 13664 through its interactions, instead of AR 13668 itself turning into a highly complex region.

The bottom panel of Figure 6 displays the soft X-ray flares occurring in the host ARs 13664/8 by red and blue bars, respectively. Halo CMEs are overlaid in blue at the top of the panel. More detailed information on the active region for each day, namely the active region area, number of sunspots, Zurich-McIntosh classification (ZMCINT), magnetic classification

---

[10] http://helio.mssl.ucl.ac.uk/helio-vo/solar_activity/arstats/arstats_page5.php?region=13664

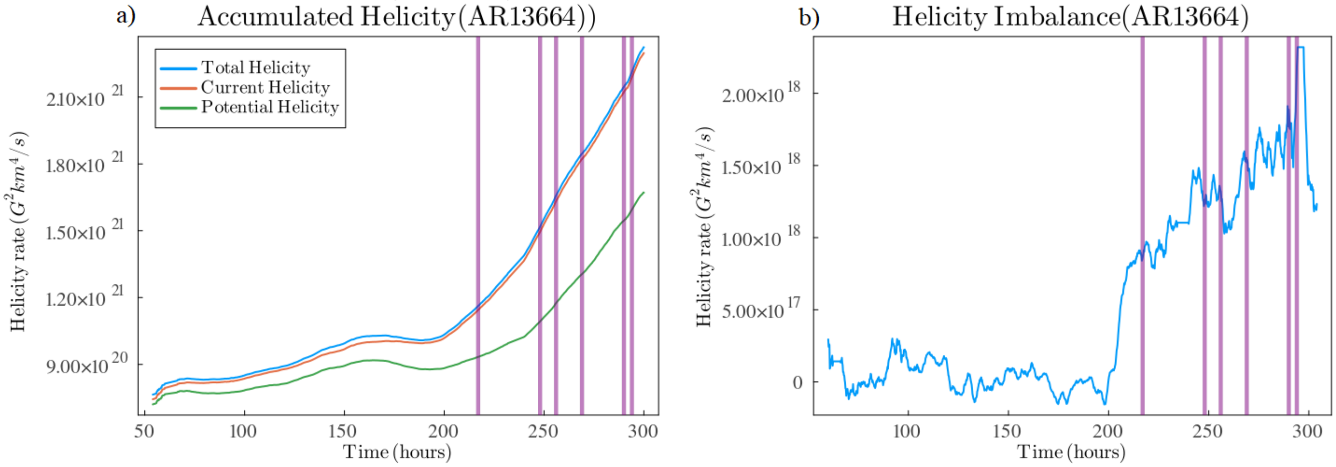

Figure 5. Evolution of the accumulated helicity (a) and the helicity imbalance (b). Panel (a) shows the increase in the helicity injection (notice the increase in the slopes of the curves) which accompanied the occurrence of the major (X-class) flares. Panel (b) shows the spikes in the helicity imbalance, indicating fast emergence of current-carrying structures which match the occurrence of the X-class flares.

(MCLASS), and the number of C-, M-, and X-class flares that have occurred as well as the total number of flares, can be found on the HELIO website (see footnote 10).

We further selected nine additional parameters, namely (i) the percentage total area with shear angle greater than 45° (SH-ANG > 45), (ii) the R-value (the flux contribution around polarity inversion lines, PILs), (iii) the S_{l-f} (the spatial separation of opposite-polarity subgroups within an active region), (iv) the total density of free magnetic energy, (v) the horizontal magnetic gradient (G_S), (vi) the total unsigned magnetic flux, (vii) the gradient-weighted integral length of the neutral line ($\mathrm{WL_{SG}}$), (viii) the main polarity inversion lines (MPILs), and (ix) the number of null points between 2 and 10 Mm. These parameters are derived from the corresponding magnetogram data using scripts made available by the FLARECAST project (M. K. Georgoulis et al. 2021),[11] and their evolution was subsequently studied. The analysis begins on May 4, when the magnetic classification starts to become complex (see Figure 6) and the accumulated helicity begins to increase (as shown in Figure 5(a), at $t \sim 100$), and continues until the end of May 11, as illustrated in Figure 5.

Each of the applied parameters (i)–(ix) offers unique insights into how and why this active region became so active. For a detailed comparative analysis of the nine selected parameters, we normalized the parameter values by dividing them by their respective maximum values. This normalization method allows us to standardize the data, making it easier to compare the evolution of different parameters, as seen in Figures 7, 8, and 9. Before comparing their evolution, we provide a brief analysis of each parameter individually.

3.2.4. Percentage Total Area with Shear Angle greater than 45°

The first parameter is the percentage of the total area where the shear angle is greater than 45° (SH-ANG > 45). The normalized evolution of SH-ANG > 45 is shown in Figure 7 with the blue line. The shear angle is defined as the angle between the observed magnetic field's orientation and that of a potential field. A shear angle exceeding 45° typically indicates significant magnetic complexity and nonpotentiality in the magnetic field configuration. This percentage provides a quantitative measure of the extent to which the region is under high magnetic tension and, consequently, its potential for increased activity or volatility (e.g., M. J. Hagyard et al. 1984; K. D. Leka & G. Barnes 2007). In the case of ARs 13664/8, over 50% of the total area exhibited a shear angle greater than 45° during the studied period.

The R-value, introduced by C. J. Schrijver (2007), quantifies the flux contribution around PILs using line-of-sight magnetograms from the Solar and Heliospheric Observatory's Michelson Doppler Imager. The R-value was determined for 289 active regions, showing a consistent correlation between large flares and regions with pronounced high-gradient polarity separation lines. Furthermore, it was observed that if the log(R-value) exceeds 5, there is a significant likelihood of large solar eruptions. During the period studied, the log(R-value) indeed exceeded 5 at all times. The normalized evolution of the R-value is shown in Figure 7 with the orange line.

The separation parameter S_{l-f}, introduced by M. B. Korsós & R. Erdélyi (2016), serves as a complexity metric for evaluating the spatial separation of opposite-polarity subgroups within an active region on the Sun. This parameter provides valuable insights into the magnetic field structure of sunspots by assessing the proximity of positive- and negative-polarity areas within a sunspot group. A decreasing S_{l-f} value indicates that the positive and negative polarities are becoming more interconnected, and the active region is becoming more polarity-mixed and complex. In Figure 7, the evolution of S_{l-f} is represented by the green line. The sudden jump in the S_{l-f} parameter on May 5 is due to the rapid emergence of AR 13668. When deriving the S_{l-f} values at each time step, strong magnetic polarity elements are considered only if their area exceeds 0.5 MSH (millionths of the solar hemisphere). At that time, the initial magnetic elements of AR 13668 appeared at a distance from AR 13664, resulting in a sharp rise in the S_{l-f} value. As AR 13668 continued to grow and eventually began to merge with AR 13664, the S_{l-f} parameter began to decrease. In the case of ARs 13664/8, this parameter decreased rapidly and then stabilized as the active region

---

[11] https://dev.flarecast.eu/stash/projects/FE

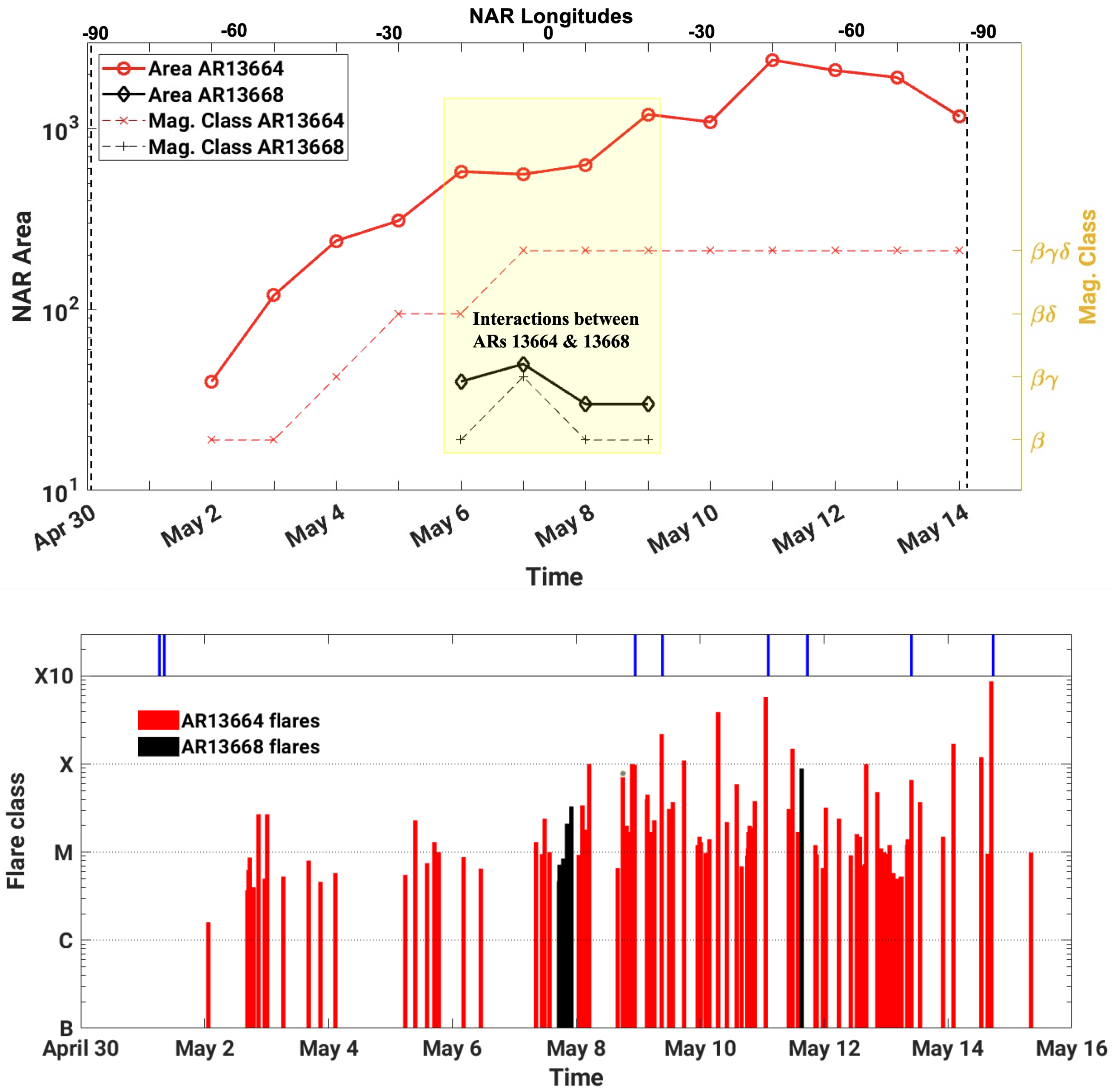

Figure 6. Top: the area evolution of AR 13364 (red) and AR 13368 (black). The longitude of the active regions is shown at the top of the corresponding plots. The vertical dashed lines mark when the active regions cross the east and west limbs. Bottom: the peak time and size of the soft X-ray flares that occurred in the host active regions (AR 13364/13368 denoted by red/black vertical lines). The times of halo CME events (width >135°) that occurred during the period are visualized as blue bars at the top of the panels. Data credits to HELIO (http://helio.mssl.ucl.ac.uk/helio-vo/solar_activity/arstats/arstats_page5.php?region=13664).

became fully developed, suggesting a steady spatial arrangement and a possible energy buildup conducive to significant solar events.

3.2.5. Free Magnetic Energy Density, Horizontal Magnetic Gradient, and Total Unsigned Magnetic Flux

The density of free magnetic energy in the photosphere is a critical metric for characterizing magnetic nonpotentiality, as discussed by J. Wang et al. (1996). Building on this concept, K. D. Leka & G. Barnes (2007) demonstrated that free (or excess) magnetic energy is a reliable parameter for predicting solar flares. Specifically, a higher total free energy in an active region significantly increases the likelihood of it producing large flares, particularly when the energy density exceeds 10^{24} erg cm^{-3}. For the studied ARs 13664/8, the density of free magnetic energy consistently exceeded 10^{24} erg cm^{-3} throughout the observation period. The normalized evolution of this parameter is shown in Figure 8 with the blue line.

The horizontal magnetic gradient G_S, introduced by M. B. Korsós & R. Erdélyi (2016), serves as a morphological parameter that quantifies the magnetic interactions within a sunspot group, especially focusing on the horizontal magnetic gradient between opposite-polarity umbrae. According to I. Kontogiannis et al. (2018), if the horizontal magnetic gradient reaches or exceeds 10^5 G pixel^{-1}, there is an increased likelihood of larger solar flares occurring. For the studied ARs 13664/8, the

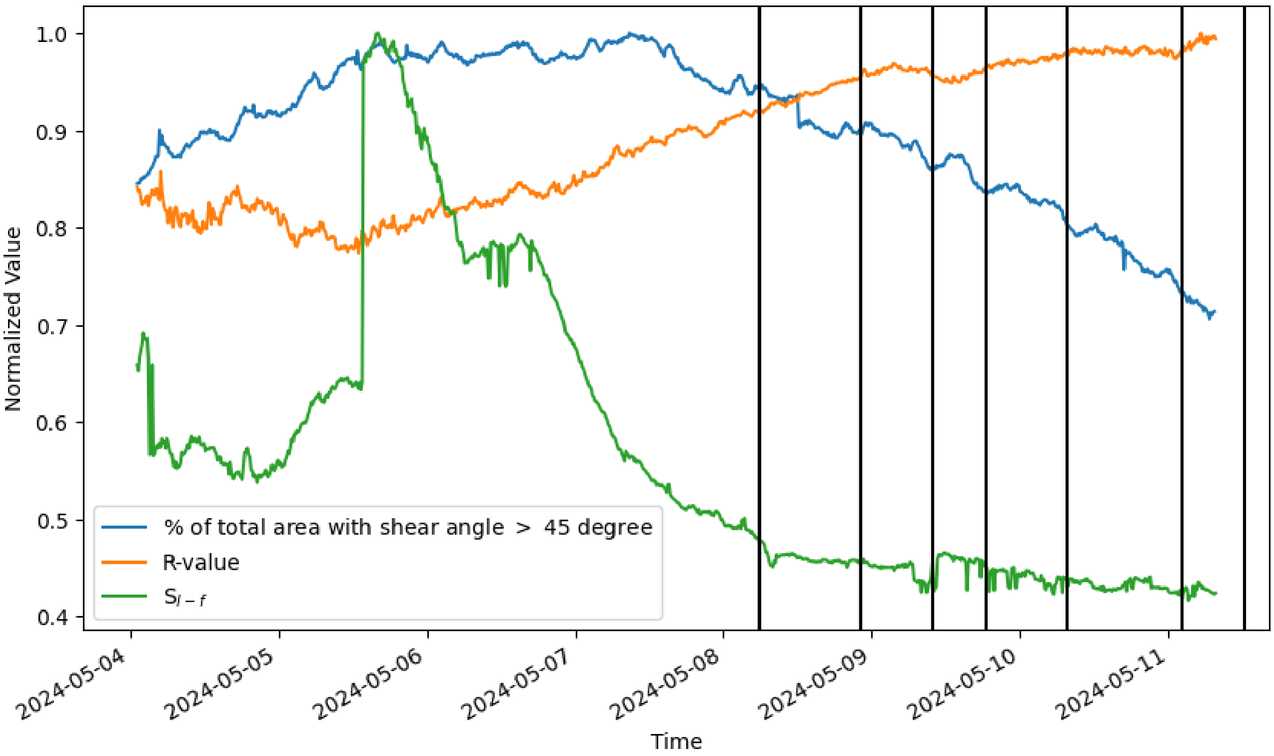

Figure 7. Percentage total area with shear angle greater than 45° (SH-ANG > 45) is displayed in blue. *R*-value (flux contribution around PILs) and the separation parameter S_{l-f} (the spatial separation of opposite-polarity subgroups within an active region) are displayed in orange and green, respectively. For comparison analysis, the parameters SH-ANG, *R*-value, and S_{l-f} have been normalized by dividing them by their respective maximum values. This approach scales each parameter to a uniform range, enhancing the accuracy and relevance of comparative studies. The black lines indicate the flares: 2024 May 8 05:09 X1.0, 2024 May 8 21:08 X1.0, 2024 May 9 09:13 X2.2, 2024 May 9 17:44 X1.1, 2024 May 10 06:54 X3.9, and 2024 May 11 01:23 X5.8. Data recorded every 12 minutes from 2024 May 4.

G_S consistently exceeded this threshold level throughout the observation period. The normalized evolution of the G_S parameter is shown in Figure 8 with the orange line.

The total unsigned magnetic flux is a critical indicator of the potential for significant solar flare activity and CMEs. Research by T. Li et al. (2021), which analyzed 719 flares of GOES class ±C5.0 from 2010 to 2019, found that active regions with magnetic flux values exceeding 10^{23} Mx are more likely to produce M- or X-class flares. This correlation highlights the role of high flux thresholds in increased active region activity. In the case of ARs 13664/8, the magnetic flux was already substantial at the start of the observation period, in the order of 10^{24} Mx, and increased to the order of 10^{25} Mx. The normalized evolution of the total unsigned magnetic flux is shown in Figure 8 with the green line.

Also, the gradient-weighted integral length of the neutral line ($\mathrm{WL_{SG}}$) is an indirect measure of the free magnetic energy in an active region. This parameter focuses on the strong-field intervals along the PIL, specifically targeting areas where the horizontal magnetic field, derived from the vertical field component of the magnetogram, exceeds 150 G. D. A. Falconer et al. (2012) concluded that if $\mathrm{WL_{SG}}$ exceeds 10^4 G, there is a 75% probability of a major solar eruption occurring within the next 24 hr. For ARs 13664/8, the $\mathrm{WL_{SG}}$ values were exceptionally high from the beginning, consistently above 10^5 G and eventually exceeding 10^6 G. These unusually high values indicate a very high potential for significant solar activity. The normalized evolution of the $\mathrm{WL_{SG}}$ parameter is shown in Figure 8 with the red line.

3.2.6. Polarity Inversion Lines and Magnetic Null Points

A polarity inversion line (PIL) marks a critical boundary within an active region, separating areas of positive and negative magnetic flux. Such lines, particularly where the magnetic field gradient is steep, signify strong shearing or twisting of the magnetic field structure. The MPIL specifically delineates the primary polarity regions of an active region. D. A. Falconer et al. (2003) investigated the predictive potential of the MPIL for CMEs, while J. P. Mason & J. T. Hoeksema (2010) demonstrated its relevance for flare prediction. They proposed that a significant solar eruption could be expected within a 2 day period if the MPIL length exceeds 62 Mm and the observed transverse field strength is greater than 150 G. For ARs 13664/8, the MPIL measurements were particularly remarkable, beginning at approximately 100 Mm at the start of the observation period and eventually extending to between 300 and 400 Mm. The normalized evolution of the MPIL parameter is shown in Figure 9 with the blue line.

Recent studies, including a notable investigation by R. L. Edgar & S. Régnier (2024), have explored the relationship between magnetic null points and solar flares, with particular focus on the elevation of these null points above the solar surface. This research, which analyzed several X-class flares during solar cycle 24, revealed that the magnetic null points associated with these flares were predominantly located in the lower solar atmosphere. In the case of ARs 13664/8, we also tracked the evolution of the number of null

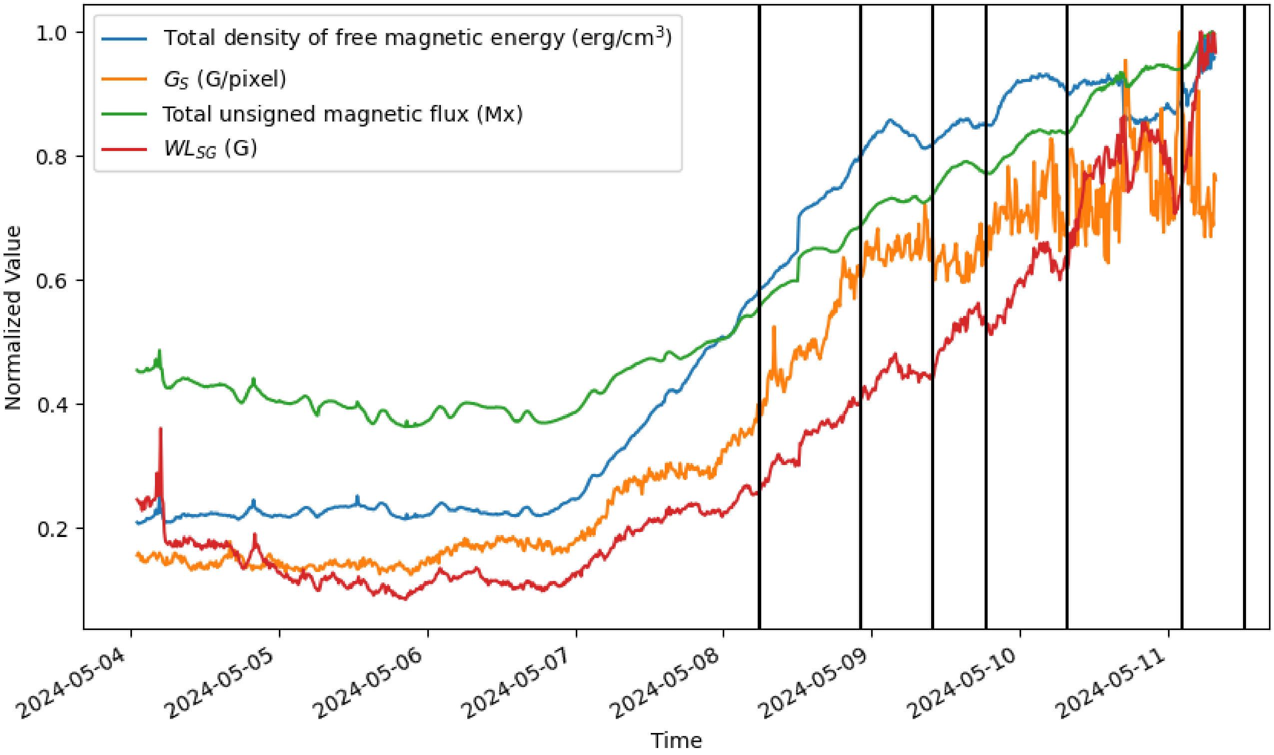

Figure 8. Total density of free magnetic energy (blue), horizontal magnetic gradient (G_S, orange), total unsigned magnetic flux (green), and gradient-weighted integral length of the neutral line ($\mathrm{WL_{SG}}$, red) are displayed; black lines overlaid on this plot indicate flares. These parameters have again been normalized as in Figure 7, i.e., by dividing them by their respective maximum values.

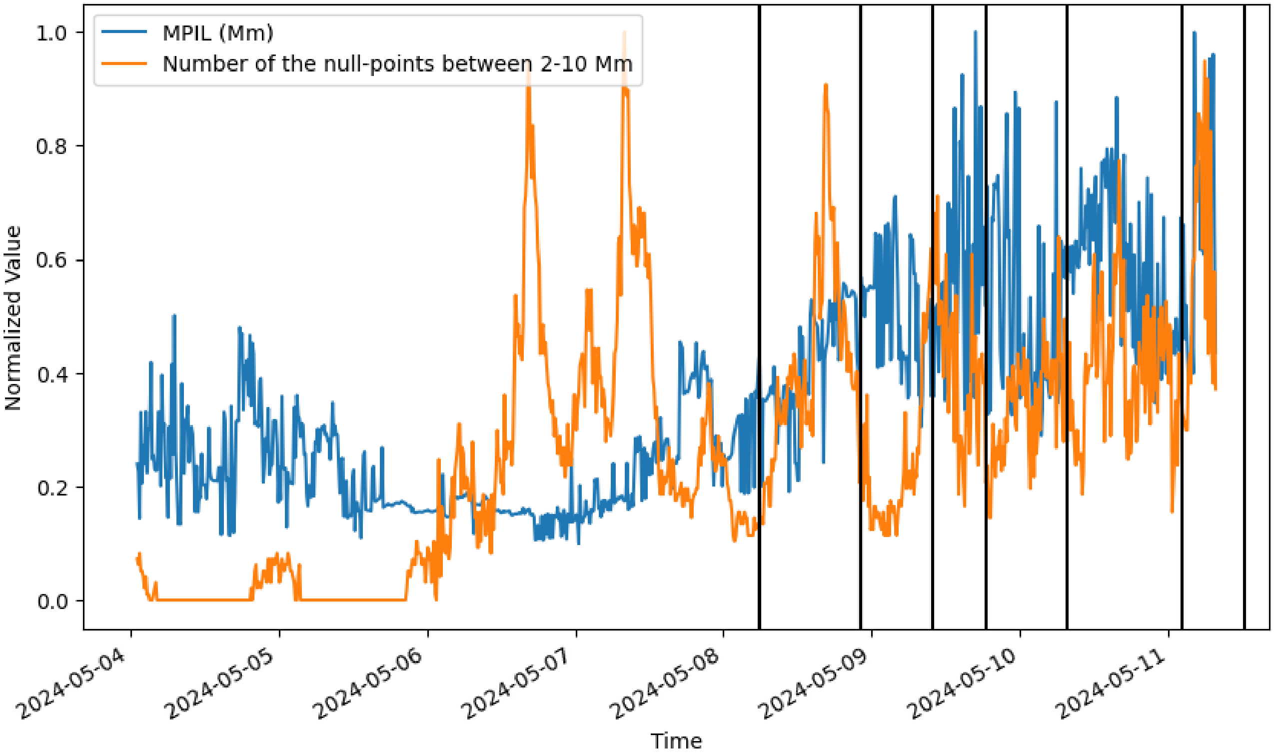

Figure 9. Main polarity inversion lines (MPILs, blue) and number of null points between 2 and 10 Mm (orange) are displayed; again, as in Figure 7, black lines indicate flares and the parameters have been normalized by dividing them by their respective maximum values.

points between 2 Mm and 10 Mm above the solar surface. The normalized evolution of the number of null points is shown with the orange line in Figure 9.

We also compared the evolution of the parameters collectively, leading to the following observations. On May 4, the parameters were already above their respective threshold levels when a small bipolar structure began to surface on the eastern flank of two preexisting bipolar magnetic structures within AR 13664. This early indication, with all parameters exceeding their thresholds, suggested that the active region stored a significant amount of free energy, which continued to accumulate, as further supported by the magnetic helicity discussed in Section 3.2.2. This newly emerged structure was designated as a separate active region, AR 13668. By May 6, another bipolar pair had developed and quickly separated from ARs 13664 and 13668, further indicating the buildup of magnetic energy. This was evidenced by changes in null points, the S_{l-f}, and the R-value, all of which signaled a complex, sheared, and dynamic magnetic field structure. On May 7, two additional bipolar magnetic structures appeared between AR 13664 and AR 13668, aligned north–south. These structures moved westward, exhibiting significant shearing, and formed a complex sunspot cluster named ARs 13664/8. The magnetic parameters—including the total free energy density, W_S, total unsigned flux, $\mathrm{WL_{SG}}$, SHANG > 45, and MPIL—showed heightened values almost simultaneously. This cluster began emitting X-class flares on May 8, producing a total of 11 X-class flares before moving beyond the Sun's western limb. The merging and interaction of these two active regions transformed ARs 13664/8 into a highly flare-productive complex.

For most of the investigated X-class flares, the evolution of the number of null points shows a peak and then returns to approximately the same level as before the flare—except for the third X-class flare on May 9, which occurred around the time of the maximum value. Meanwhile, the rest of the parameters continued to evolve, either increasing or decreasing in their respective gradients, highlighting the dynamic nature of this highly active region.

4. Summary and Conclusions

Our goal in this paper has been to analyze both global warped toroid and active-region-scale magnetic patterns of the well-known "Mother's Day" superstorms, to understand how the different scales in longitude and time connect, and look for features in the global toroid patterns that might help predict the eruption of new active regions in the following few weeks or even months.

On the global scale, we have found that the toroids we have fitted to synoptic magnetograms evolved slowly in the month or two before the superstorm. The north and south toroids have nearly identical warped patterns, with dominant strength in longitudinal wavenumbers $m = 1, 2, 3$. The phases in longitude of the patterns are such that there are three longitude intervals where the N and S toroids are tipped away from each other in latitude. It is these longitude intervals that seem to be more prone to the active region eruptions that are seen. We speculate that the other longitude intervals, where the toroids are tipped toward each other, are less likely to be sites of new active regions, because there is some flux reconnection between hemispheres going on there, much deeper down in the convection zone or the tachocline.

This picture is made more complex by the fact that in the south near 350° longitude there was a decaying active region that produced more complex interactions when the new active region emerged. We have additional confidence in our toroid fits because they are similar when derived separately from SDO/HMI and GONG magnetograms. GONG-based toroids are slightly wider in latitude than those from SDO/HMI, because the spatial resolution of GONG is substantially coarser.

Considering the local dynamics of the active regions that produced the Mother's Day superstorms, there are several previously defined indices of magnetic field amplitude, structure, and complexity that indicate stored magnetic energy is available for intense storms including high-powered flares. In particular, much of the vector magnetic fields deviate far from potential fields, as measured by "shear angles" of field that exceed 45°. These regions therefore also contain large amounts of magnetic "free energy" available for conversion into kinetic energy and high-temperature radiation. In addition, there are particularly strong fields very close to PILs as defined by line-of-sight magnetograms, implying very strong horizontal magnetic field gradients there.

Furthermore, the configurations are dynamic, with positive and negative polarities converging toward each other, facilitating reconnection and magnetic energy release. The total unsigned magnetic flux is another indicator of likely flare activity, and these active regions have very large total unsigned flux. The length of the horizontal neutral line is still another indicator; the Mother's Day active regions have unusually long such neutral lines. Relatedly, the length of the magnetic neutral line is another indicator of magnetic shearing that can lead to eruptions. These active regions showed substantial lengthening of this neutral line prior to the eruptions.

We can conclude that the main cause of the intensity of the Mother's Day superstorms can be attributed to enhanced magnetic complexity resulting from intricate interactions among multiple active regions emerging at the same locations or in close proximity. While this type of "rogue" active region is rare (M. Nagy et al. 2017), it already possesses a level of magnetic complexity sufficient to produce major solar eruptions. However, it is still important to study such regions using different proxy parameters to determine when they are actively preparing themselves physically for eruption. This analysis suggests that predicting the locations of magnetically complex active regions—and studying their evolution through various proxy parameters—can greatly enhance our ability to forecast intense storms, not just hours but potentially weeks in advance.

The obvious next question is: How are the location and temporal evolution of an active region physically related? Are there clues in the global toroids that could predict when, where, and with what strength the active regions would emerge? How often do they emerge at the location of existing active regions? Because the complex interactions among the multiple emergences at the same or in close neighboring regions are essentially the progenitors of the biggest classes CMEs and flares, it is the burning issue to investigate and find out the physical foundation of recurrent emergences and the formation of so-called "activity nests."

Acknowledgments

We thank an anonymous reviewer for a very thorough review and for many helpful comments, taking care of which significantly improved our paper. This work is supported by the NSF National Center for Atmospheric Research, which is a major facility sponsored by the National Science Foundation (NSF) under cooperative agreement 1852977. M.D. acknowledges partial support from various NASA grants, such as NASA-LWS award 80NSSC20K0355 (awarded to NCAR), and NASA-HSR award 80NSSC21K1676 (awarded to NCAR). M.D., A.N., B.R., and K.J. acknowledge partial support from NASA-DRIVE Center award 80NSSC22M0162 to Stanford. B.R. also acknowledges support from by FAPESP (processes 23/16513-9 and 24/20546-2). M.B.K. acknowledges NKFIH (OTKA, grant No. K142987) Hungary and the UK Leverhulme Trust Found ECF-2023-271. This work also utilizes GONG data obtained by the NSO Integrated Synoptic Program, managed by the National Solar Observatory, which is operated by the Association of Universities for Research in Astronomy (AURA), Inc. under a cooperative agreement with the National Science Foundation and with contribution from the National Oceanic and Atmospheric Administration (NOAA). The GONG network of instruments is hosted by the Big Bear Solar Observatory, High Altitude Observatory, Learmonth Solar Observatory, Udaipur Solar Observatory, Instituto de Astrofísica de Canarias, and Cerro Tololo Interamerican Observatory. This work also utilizes data from HMI on board NASA's SDO spacecraft, courtesy of NASA/SDO and the HMI Science Teams.

Facilities: GONG, SDO, GOES.

ORCID iDs

Mausumi Dikpati https://orcid.org/0000-0002-2227-0488
Marianna B. Korsós https://orcid.org/0000-0002-0049-4798
Aimee A. Norton https://orcid.org/0000-0003-2622-7310
Breno Raphaldini https://orcid.org/0000-0002-0744-9746
Kiran Jain https://orcid.org/0000-0002-1905-1639
Scott W. McIntosh https://orcid.org/0000-0002-7369-1776
Peter A. Gilman https://orcid.org/0000-0002-1639-6252
Andre S. W. Teruya https://orcid.org/0000-0001-5113-7937
Nour E. Raouafi https://orcid.org/0000-0003-2409-3742

References

Berger, M. A. 1999, PPCF, 41, B167
Berger, M. A., & Field, G. B. 1984, JFM, 147, 133
Bobra, M. G., & Couvidat, S. 2015, ApJ, 798, 135
Bobra, M. G., & Ilonidis, S. 2016, ApJ, 821, 127
Branch, M. A., Coleman, T. F., & Li, Y. 1999, SJSC, 21, 1
Cally, P. S., Dikpati, M., & Gilman, P. A. 2003, ApJ, 582, 1190
Dikpati, M., & McIntosh, S. W. 2020, SpWea, 18, e02109
Dikpati, M., McIntosh, S. W., Chatterjee, S., et al. 2021, ApJ, 910, 91
Edgar, R. L., & Régnier, S. 2024, MNRAS, 532, 755
Elsasser, W. M. 1956, RvMP, 28, 135
Falconer, D. A., Moore, R. L., Barghouty, A. F., & Khazanov, I. 2012, ApJ, 757, 32
Falconer, D. A., Moore, R. L., & Gary, G. A. 2003, JGRA, 108, 1380
Georgoulis, M. K., Bloomfield, D. S., Piana, M., et al. 2021, JSWSC, 11, 39
Hagyard, M. J., Smith, J. B., Jr., Teuber, D., & West, E. A. 1984, SoPh, 91, 115
Hale, G. E., Ellerman, F., Nicholson, S. B., & Joy, A. H. 1919, ApJ, 49, 153
Hayakawa, H., Ebihara, Y., Mishev, A., et al. 2025, ApJ, 979, 49
Jaeggli, S. A., & Norton, A. A. 2016, ApJL, 820, L11
Kontogiannis, I., Georgoulis, M. K., Park, S.-H., & Guerra, J. A. 2018, SoPh, 293, 96
Korsós, M. B., & Erdélyi, R. 2016, ApJ, 823, 153
Kruparova, O., Krupar, V., Szabo, A., et al. 2024, ApJL, 970, L13
Leka, K. D., & Barnes, G. 2007, ApJ, 656, 1173
Li, T., Chen, A., Hou, Y., et al. 2021, ApJL, 917, L29
Li, Y., Liu, X., Jing, Z., et al. 2024, ApJL, 972, L1
Liokati, E., Nindos, A., & Georgoulis, M. K. 2023, A&A, 672, A38
Liokati, E., Nindos, A., & Liu, Y. 2022, A&A, 662, A6
Liu, Y. D., Hu, H., Zhao, X., Chen, C., & Wang, R. 2024, ApJL, 974, L8
MacTaggart, D., & Prior, C. 2021, GApFD, 115, 85
MacTaggart, D., & Valli, A. 2023, JPhA, 56, 435701
Mason, J. P., & Hoeksema, J. T. 2010, ApJ, 723, 634
Miesch, M. S., Gilman, P. A., & Dikpati, M. 2007, ApJS, 168, 337
Nagy, M., Lemerle, A., Labonville, F., Petrovay, K., & Charbonneau, P. 2017, SoPh, 292, 167
Norton, A. A., & Gilman, P. A. 2005, ApJ, 630, 1194
Raphaldini, B., Dikpati, M., Norton, A. A., et al. 2023, ApJ, 958, 175
Raphaldini, B., Dikpati, M., Teruya, A. S. W., et al. 2024, A&A, 691, A3
Raphaldini, B., Prior, C. B., & MacTaggart, D. 2022, ApJ, 927, 156
Romano, P., Elmhamdi, A., Marassi, A., & Contarino, L. 2024, ApJL, 973, L31
Schrijver, C. J. 2007, ApJL, 655, L117
Toriumi, S., & Park, S.-H. 2024, in Helicities in Geophysics, Astrophysics, and Beyond, ed. K. Kuzanyan et al. Vol. 283 (New York: Wiley), 83
Wang, J., Shi, Z., Wang, H., & Lue, Y. 1996, ApJ, 456, 861